

Momentum-resolved lattice dynamics of parent and electron-doped Sr₂IrO₄

C. D. Dashwood,^{1,*} H. Miao,² J. G. Vale,¹ D. Ishikawa,³ D. A. Prishchenko,⁴ V. V. Mazurenko,⁴ V. G. Mazurenko,⁴ R. S. Perry,¹ G. Cao,⁵ A. de la Torre,^{6,7} F. Baumberger,⁷ A. Q. R. Baron,³ D. F. McMorrow,¹ and M. P. M. Dean²

¹London Centre for Nanotechnology and Department of Physics and Astronomy,
University College London, Gower Street, London WC1E 6BT, UK

²Department of Condensed Matter Physics and Materials Science,
Brookhaven National Laboratory, Upton, New York 11973, USA

³Materials Dynamics Laboratory, RIKEN SPring-8 Center, RIKEN, Sayo Hyogo 697-5148, Japan

⁴Department of Theoretical Physics and Applied Mathematics,
Ural Federal University, 19 Mira Street, Ekaterinburg 620002, Russia

⁵Department of Physics, University of Colorado at Boulder, Boulder, Colorado 80309, USA

⁶Institute for Quantum Information and Matter and Department of Physics,
California Institute of Technology, Pasadena, California 91125, USA

⁷Department of Quantum Matter Physics, University of Geneva,
24 Quai Ernest-Ansermet, 1211 Geneva 4, Switzerland

(Dated: December 15, 2024)

The mixing of orbital and spin character in the wavefunctions of the 5d iridates has led to predictions of strong couplings between their lattice, electronic and magnetic excitations. As well as realising a novel spin-orbit assisted Mott insulating ground state, the perovskite iridate Sr₂IrO₄ has been shown to have strong similarities with the cuprate La₂CuO₄, which on doping hosts many broken symmetry phases such as charge density waves that appear to be intimately linked to high-temperature superconductivity. These phenomena can be sensitively probed through momentum-resolved measurements of the lattice dynamics, made possible by meV-resolution inelastic x-ray scattering. Here we report the first such measurements for parent and electron-doped Sr₂IrO₄, which we interpret with the help of density functional theory calculations and contrast with the phonon behaviour of the underdoped cuprates.

I. INTRODUCTION

The delicate balance of spin-orbit coupling (SOC), crystal fields and electron correlations (U) in the 5d iridates makes them a fruitful class of materials in the search for novel electronic and magnetic phases¹⁻⁴. Most prominently, the layered perovskite Sr₂IrO₄ has been shown to be a spin-orbit Mott insulator where the orbital degeneracy of the Ir⁴⁺ t_{2g} levels is lifted by SOC, enabling a moderate $U \sim 2$ eV to open a charge gap^{5,6}. Moreover, it has striking structural, electronic and magnetic similarities to the parent of the cuprate high-temperature superconductors La₂CuO₄⁷⁻¹⁰. Doping the bulk of Sr₂IrO₄ with electrons leads to the suppression of long-range antiferromagnetic order¹¹, while surface-doping has been shown to produce Fermi arcs¹² and a low-temperature gap with d -wave symmetry¹³.

One difference from the cuprates is the orbital character of the $j_{\text{eff}} = 1/2$ wavefunction, which results in the couplings between the pseudospins being highly sensitive to lattice geometry¹. Recent theoretical¹⁴ and experimental¹⁵ work has shown that this coupling is crucial to understanding the magnetic structure and in-plane magnon gap of Sr₂IrO₄. Lattice distortions can result in significant admixture of the $j_{\text{eff}} = 3/2$ wavefunction into the $j_{\text{eff}} = 1/2$ ground state, which has led to expectations of strong interactions between lattice, orbital, and magnetic excitations in the layered iridates. For example, Gretarsson *et al.*¹⁶ conducted Raman measurements on Sr₂IrO₄, finding Fano asymmetry in the A_{1g} phonon

mode above $T_N \approx 240$ K, that is indicative of coupling between the lattice and a continuum of pseudospin fluctuations due to unquenched orbital dynamics.

A notable feature of the underdoped cuprates is the appearance of charge density wave (CDW) order above a critical doping, which appears to be connected to the superconductivity in these compounds^{17,18}. CDW order has long been proposed to be an intrinsic instability of doped Mott insulators^{19,20}, but despite reports of spin density wave order²¹ in doped Sr₂IrO₄ and a dynamic CDW-like instability in its bilayer cousin Sr₃Ir₂O₇^{22,23}, as yet there has been no evidence for a CDW in doped Sr₂IrO₄. The presence of CDW order can be inferred, *inter alia*, from the softening of phonon modes around the CDW wavevector²⁴⁻²⁶.

There is therefore a clear interest in momentum-resolved measurements of the phonons in the iridates. Non-resonant inelastic x-ray scattering (IXS) is a suitable probe to accomplish this, offering ~ 1 meV energy resolution and ~ 0.01 r.l.u. momentum resolution across a large volume of reciprocal space²⁷. We have performed extensive IXS measurements on parent and La-doped Sr₂IrO₄, comparing the results with density functional theory (DFT) calculations. In the parent compound, we find that our IXS spectra are reasonably reproduced by a non-magnetic DFT calculation, with no broadening or frequency shifts apparent through T_N . We observe minimal changes to the phonons on doping, with the dispersions again well-reproduced by DFT, and no anomalies apparent at the equivalent cuprate CDW wavevector.

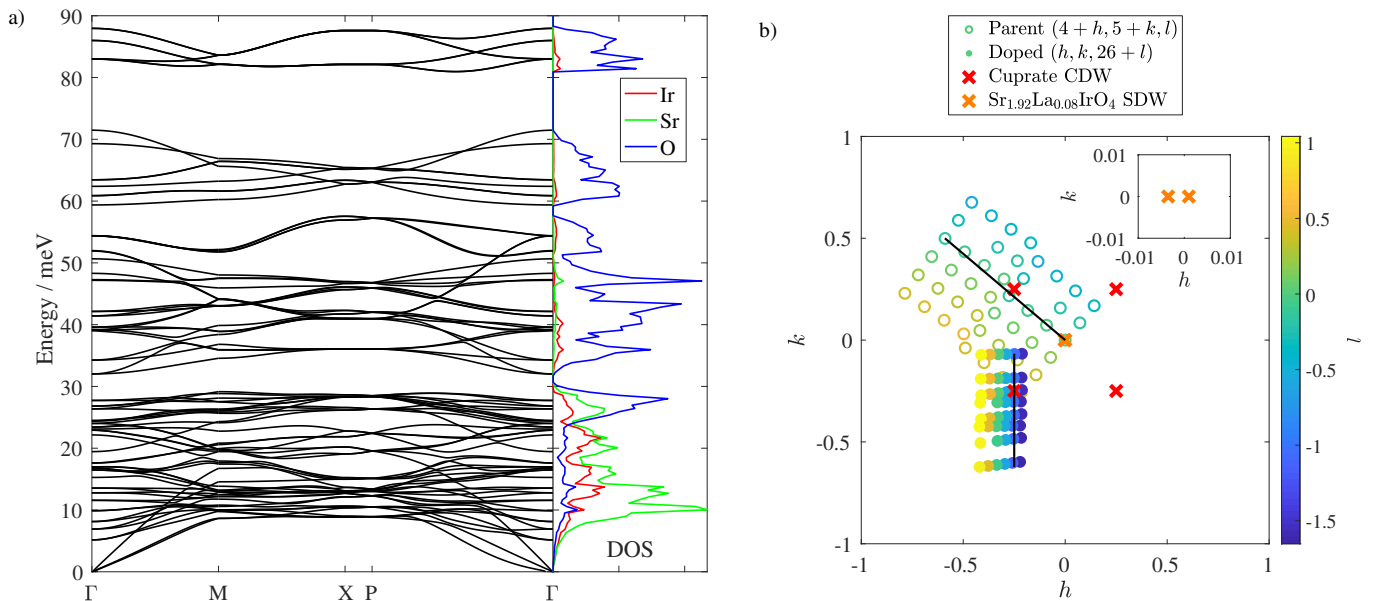


FIG. 1. a) Phonon band structure (black lines) and projected phonon DOS for Ir (red), Sr (green) and O (blue), calculated in the LDA approximation on a $2 \times 2 \times 1$ supercell. The high-symmetry points of the $I4_1/acd$ space group are defined as $\Gamma = (0, 0, 0)$, $M = (0.5, 0, 0)$, $X = (0.5, 0.5, 0)$, and $P = (0.5, 0.5, 0.5)$. b) Brillouin zone map (structural and magnetic zones are equivalent in the $I4_1/acd$ notation) showing the measured \mathbf{Q} points for the parent compound relative to $(4, 5, 0)$ as empty circles, and for the doped compound relative to $(0, 0, 26)$ as filled circles. The points have been projected onto the $h-k$ plane, with l values indicated by colour. The red crosses show the equivalent in-plane wavevector of the cuprate CDW²⁶ and orange crosses those of the purported SDW in doped Sr_2IrO_4 ²¹ (shown magnified in the inset). The black lines indicate the reciprocal space directions for which data is shown in this manuscript, with spectra at the other \mathbf{Q} points contained in the supplemental material.

II. METHODS

Single crystals of both parent ($x = 0$) and 5% doped ($x \approx 0.05$) $(\text{Sr}_{1-x}\text{La}_x)_2\text{IrO}_4$ were flux grown using standard methods and characterised by energy-dispersive x-ray spectroscopy, resistivity and susceptibility measurements²⁸. The crystalline quality of the samples was checked during the IXS measurements, with mosaics of around 0.02° for the parent compound and 0.05° for the doped. Throughout this manuscript, the \mathbf{Q} vectors are referenced to the $I4_1/acd$ space group with $a = b = 5.50 \text{ \AA}$ and $c = 25.79 \text{ \AA}$.

DFT calculations were performed using the plane-wave basis projector augmented wave (PAW) method²⁹ as implemented in the Vienna *ab-initio* Simulation Package (VASP)³⁰. The exchange-correlation functional was treated in the Local Density Approximation (LDA)³¹, with unit cell relaxations carried out over an $8 \times 8 \times 2$ reciprocal lattice mesh. The force constants were calculated over a $4 \times 4 \times 2$ mesh using a $2 \times 2 \times 1$ supercell. The phonon frequencies and eigenvectors were then obtained using the PHONOPY package³² with an $11 \times 11 \times 11$ mesh for the Debye-Waller factor, and these were used to calculate the dynamic structure factor $S(\mathbf{Q}, \omega)$ (see supplemental material). The resulting phonon band structure and projected density of states (DOS) is shown in Fig. 1a. As expected, the modes involving motion of mostly the

heavier Sr and Ir atoms lie at lower energies, while the modes involving lighter O atoms dominate above 30 meV.

Calculations were also performed including the effects of SOC+U with the full non-collinear magnetic structure³³, but the computational complexity of this meant that the supercell size had to be reduced to the point where agreement between the calculated dynamic structure factor and IXS spectra became unsatisfactory (see the appendix for further discussion).

High-resolution IXS measurements of the phonon dispersions were performed at beamline BL43LXU of the SPring-8 synchrotron in Japan³⁴. The incident energy was set to 21.75 keV and the $(11, 11, 11)$ reflection of Si was used as both a monochromator and analyser, giving an energy resolution of around 1.5 meV (depending on analyser). A 4×6 analyser array allowed the simultaneous measurement of many momentum transfers, so that a large area of the Brillouin zone, shown in Fig. 1b, could be surveyed despite the long counting times necessitated by the high energy and momentum resolutions.

The parent compound was measured in transmission with the $[1, 1, 0]$ and $[0, 0, 1]$ reciprocal directions in the scattering plane, allowing access to purely in-plane momentum transfers in order to maximise the intensity of modes that involve modulation of the Ir-O-Ir superexchange bond. The vertical columns of the analyser array traced out adjacent trajectories along $[\bar{1}, 1, 0]$ out from

the $(5, 4, 0)$ magnetic Bragg peak position (open circles in Fig. 1b). As well as avoiding points near the structural Bragg peaks $(4, 4, 0)$ and $(4, 6, 0)$ at which the IXS spectra would be dominated by strong elastic contributions (which does not occur at the magnetic Bragg peak as we are off resonance), this is also the direction along which the dynamic CDW is expected in $\text{Sr}_3\text{Ir}_2\text{O}_7$.²³ The atomic displacements of modes with significant IXS intensity were calculated using DFT for a range of other \mathbf{Q} points in the $a - b$ plane, but no modes could be found with significantly larger modulation of the Ir-O-Ir bond that we would expect to be more strongly influenced by magnetism. The black lines in Fig. 1b indicate the points with equal l for which spectra are shown in this manuscript. Spectra for the other points are contained in the supplemental material.

In the cuprates it was found that the CDW couples most strongly to modes with large c -axis displacements²⁶, which are enhanced by having a large out-of-plane momentum transfer. For the doped iridate sample we therefore used a reflection geometry with the $[1, 0, 0]$ and $[0, 0, 1]$ directions in the scattering plane, so that we could measure \mathbf{Q} points in the $(0, 0, 2\pi)$ Brillouin zone (filled circles in Fig. 1b). A vertical column of the analyser array then followed the $[0, \bar{1}, 0]$ direction (black line) through the equivalent cuprate CDW in-plane wavevector $(-0.25, -0.25)$ (filled red circles).

A consequence of the analyser geometry is that the c -axis momentum transfer, l , varies horizontally across the array as indicated by the colour of the points in Fig. 1b. The layered nature of Sr_2IrO_4 , however, means that the electronic³⁵ and magnetic⁹ behaviour of interest is only weakly l -dependent. We therefore set the analyser slits to 40×80 mm to improve the in-plane momentum resolutions while relaxing the out-of-plane resolution. The momentum resolutions are reported below for each set of measurements.

Other \mathbf{Q} points where one might expect the presence of phonon anomalies is at the intersections of the phonon and magnon dispersions. Unfortunately, the high spin-wave velocity and slight gap¹¹ places it at energies above those of the phonon modes with significant IXS intensity measured in this work.

III. RESULTS

A. Parent compound

Figure 2 shows a series of representative IXS spectra along the $[\bar{1}, 1, 0]$ direction out from the magnetic Bragg peak position $(4, 5, 0)$ in the parent compound at 100 K. The average momentum resolutions along each direction are $\delta\mathbf{Q} = (0.06, 0.07, 0.13)$ r.l.u. The IXS spectra (black points) are overlaid with $S(\mathbf{Q}, \omega)$ calculated with DFT in the LDA on a $2 \times 2 \times 1$ supercell (red lines). At all momenta, the calculation reproduces the relative intensities of the modes reasonably well, with the consistent

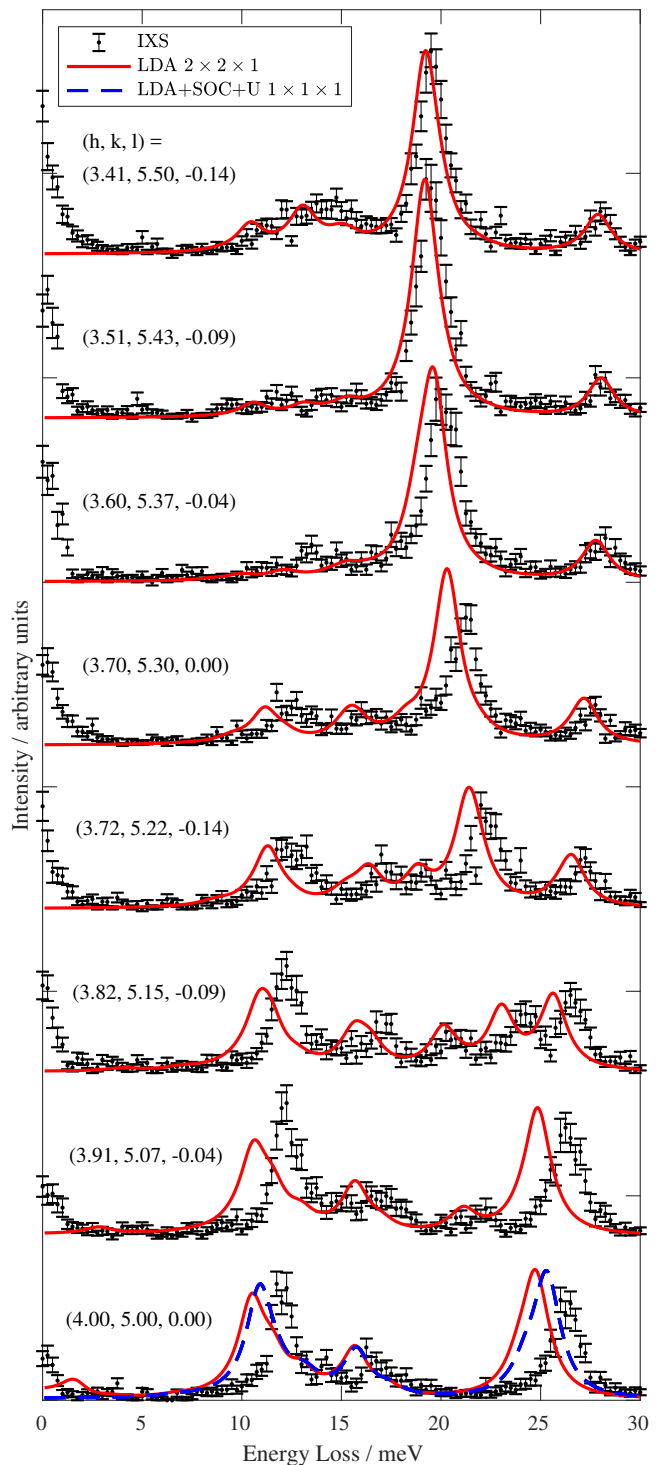


FIG. 2. Representative IXS spectra at momenta along $[\bar{1}, 1, 0]$ out from the magnetic Bragg peak position at $(4, 5, 0)$ in the parent compound at 100 K (black points) compared to $S(\mathbf{Q}, \omega)$ calculated with DFT in the LDA on $2 \times 2 \times 1$ supercell (solid red lines) and LDA+SOC+U on a $1 \times 1 \times 1$ supercell at the zone center (blue dashed line). While the LDA calculation matches the measured intensities well across the Brillouin zone, it underestimates the mode energies towards the zone center. The spectra are offset vertically for clarity.

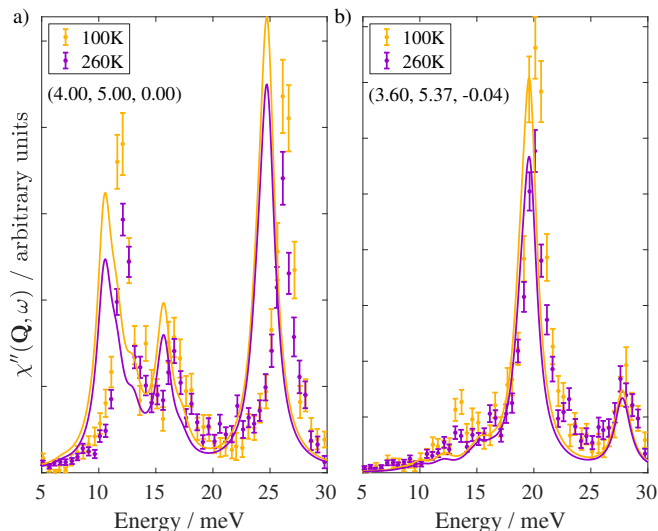


FIG. 3. Bose-factor corrected IXS spectra in the parent compound (points) and $\chi''(\mathbf{Q}, \omega)$ calculated with DFT in the LDA on $2 \times 2 \times 1$ supercell (solid lines) at 100 K (orange) and 260 K (purple) for momentum transfers of a) (4, 5, 0) and b) (3.60, 5.37, -0.04). There is no apparent softening or changes in linewidth for any of the modes.

underestimate of the mode frequencies improving further out into the Brillouin zone.

The calculation allows us to identify the atomic motion associated with each prominent peak of the IXS spectra. As expected from the in-plane momentum transfer, the modes mostly involve atomic motions in the $a - b$ plane. At the zone center, the prominent mode with an LDA energy of 10.5 meV has large displacements of the Sr atoms with smaller Ir and O motion, while the mode at 24.7 meV has dominant in-plane O motion along with smaller out-of-plane Sr oscillations. Towards the zone boundary, the mode around 19 meV has roughly equal in-plane displacements of all atoms. Animations of these modes can be found in the supplemental material.

While there is unlikely to be any detectable influence from magnetism on the low-energy mode with dominant Sr motion, the higher energy zone-center mode involves significant changes to the angle of the Ir-O-Ir bond that is responsible for magnetic superexchange. There are no apparent discrepancies between the experimental data and calculated spectrum for the high energy mode that are not also present for the low energy mode, however.

We performed DFT calculations including SOC+U with the full magnetic structure of Sr_2IrO_4 . At the zone center, where supercell size should make a minimal difference (see the appendix for further discussion), this simply causes a ~ 0.5 meV increase in the predicted energies of both modes with very little change to the intensities (blue dashed line in Fig. 2).

We repeated these measurements at 260 K, above $T_N \approx 240$ K, in order to search for any changes caused by long-range magnetic ordering. To reliably compare

spectra at different temperatures, the imaginary part of the dynamic susceptibility was calculated by subtracting the elastic line and dividing through by the Bose factor²⁶

$$\chi''(\mathbf{Q}, \omega) = S(\mathbf{Q}, \omega) \left(1 - e^{-\hbar\omega/(k_B T)}\right). \quad (1)$$

Figure 3 shows χ'' at 100 K and 260 K for two different representative momentum transfers. The intensity of the modes in the 260 K spectra are lower than those at 100 K due to the reduced Debye-Waller factor, as can be seen through comparison with $\chi''(\mathbf{Q}, \omega)$ calculated with DFT. The observed hardening of the phonon modes of ~ 0.5 meV can be attributed to reduced anharmonic phonon-phonon interactions upon cooling. There is no clear evidence for changes in the linewidth through T_N , as seen in Raman measurements by Gretarsson *et al.*¹⁶ which would be indicative of coupling to spin fluctuations. Although the asymmetric broadening of the A_{1g} mode at 23 meV reported by Gretarsson *et al.*¹⁶ is of a magnitude comparable to our energy resolution, and would therefore be visible in our data, it should be noted that this particular mode has vanishing IXS intensity at the \mathbf{Q} points measured here.

The spectra and temperature comparisons for the other momentum transfers shown in Fig. 1c can be found in the supplemental material. The same conclusions discussed above can be made for all of these data sets.

B. Doped compound

In the cuprates, a signature of the presence of CDW order is the softening and linewidth changes of phonon peaks in IXS spectra at the CDW wavevector. IXS measurements on $(\text{La}_{1-x}\text{Ba}_x)_2\text{CuO}_4$ with $x = 0.048 - 0.063$ revealed that precursor CDW fluctuations are responsible for a broadening and softening of the phonon modes^{25,26,36-41}. On the onset of CDW ordering the softening is still present while there is a sharp reduction in the phonon linewidths.

To investigate whether CDW order is present in electron-doped Sr_2IrO_4 in analogy with the hole-doped cuprates, we performed IXS measurements on 5% La-doped Sr_2IrO_4 along the $[0, \bar{1}, 0]$ direction through $(-0.25, -0.25, 25)$ with average momentum resolutions of (0.04, 0.04, 0.36) r.l.u. In order to extract the phonon dispersions, the IXS spectra were fitted to a sum of damped harmonic oscillator lineshapes χ''_j weighted by the Bose factor and convoluted with a Voigt resolution function R

$$S(\mathbf{Q}, \omega) = \sum_j \frac{\chi''_j(\mathbf{Q}, \omega)}{1 - e^{-\hbar\omega/(k_B T)}} * R(\omega) \quad (2)$$

plus an additional Voigt function for the quasi-elastic peak (see supplemental material for a representative fit). The fitted dispersions at 250 K and 9 K are shown in Fig. 4 as white and red circles respectively, overlaid on a colourmap of $S(\mathbf{Q}, \omega)$ from the same LDA calculation on a $2 \times 2 \times 2$ supercell as above.

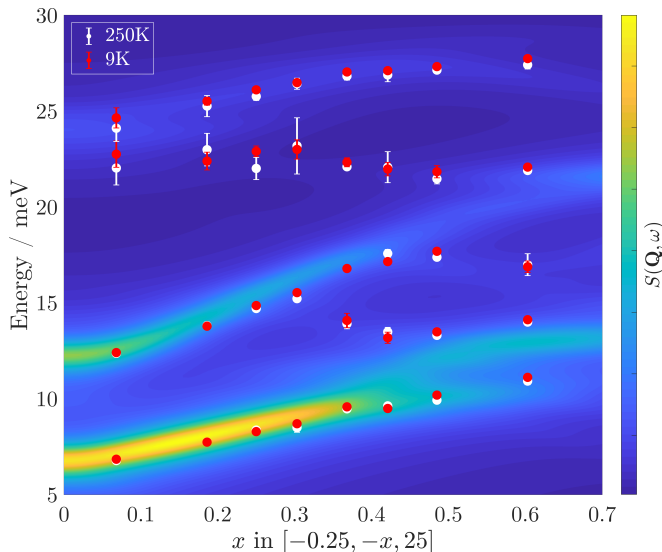


FIG. 4. Phonon dispersions at 250 K (white circles) and 9 K (red circles) extracted from fits to the IXS spectra of the doped compound. These are overlaid on a colourmap of the dynamic structure factor calculated with DFT in the LDA on $2 \times 2 \times 1$ supercell. Vertical error bars represent the statistical errors from fitting. The dispersions are identical within error at the two temperatures, with no apparent softening, and agree well with the calculation.

This non-magnetic DFT calculation actually provides a better description of the metallic ground state of the doped sample, in which long-range magnetic order is destroyed by the free carriers¹¹, and so as expected there is good agreement between the fitted and calculated dispersions. As for the parent compound, the calculations allow us to identify the atomic motions associated with each mode, which at these wavevectors involve significant out-of-plane displacements for all three elements.

Crucially, the fitted dispersions are identical (within one standard deviation) at both temperatures, with no anomalies present at the equivalent in-plane wavevector $(-0.25, -0.25)$ to the cuprate CDW. Anomalies are also not apparent at any other \mathbf{Q} points measured in this work (see supplemental material). It should be noted, however, that this does not preclude the presence of a CDW for other doping levels (the purported spin density wave only occurs over a very narrow doping range²¹), at wavevectors away from those measured here, or one that couples to a phonon modes with low IXS intensity.

A further signature of CDW order in the cuprates is visible in the intensity of the quasi-elastic peak centred at zero energy in the IXS spectra. Le Tacon *et al.*⁴² saw a contribution to the integrated intensity of this peak in the underdoped cuprate $\text{YBa}_2\text{Cu}_3\text{O}_{6.6}$ over a narrow momentum range around the CDW wavevector and over a broad temperature range around the CDW transition temperature. At both 9 K and 250 K, however, the fitted integrated intensity of the quasi-elastic peak in our IXS spectra varies smoothly with \mathbf{Q} .

IV. CONCLUSIONS

We have conducted momentum-resolved measurements of the phonons in parent and electron-doped Sr_2IrO_4 , surveying large areas of reciprocal space carefully chosen to maximise any influence from magnetic or CDW order. In both compounds, our IXS spectra are reasonably well reproduced by a non-magnetic DFT calculation in the LDA, despite the destruction of the spin-orbit assisted Mott insulating electronic and long-range ordered antiferromagnetic ground state in the latter. In the parent compound, there are no apparent changes in mode frequencies or linewidths on passing through the Néel temperature, with our data placing an upper limit on the broadening due to pseudospin-lattice coupling at around 0.3 meV. In the doped compound, the dispersion of the phonon modes along $[0, \bar{1}, 0]$ is identical within our resolution at both 9 K and 250 K, again with no softening or linewidth changes apparent nor any peaks in the quasi-elastic intensity.

ACKNOWLEDGMENTS

C. D. D. would like to thank Atsushi Togo for assistance with the PHONOPY calculations. C. D. D. was supported by the Engineering and Physical Sciences Research Council (EPSRC) Centre for Doctoral Training in the Advanced Characterisation of Materials under Grant No. EP/L015277/1. The IXS measurements were supported by the U. S. Department of Energy (DOE), Office of Basic Energy Sciences, Early Career Award Program under Award No. 1047478. The DFT calculations were carried out using high performance computing resources at Moscow State University⁴³. Work at Brookhaven National Laboratory was supported by the U. S. DOE, Office of Science, Office of Basic Energy Sciences, under Contract No. DE-SC00112704. Work at UCL was supported by the EPSRC under Grants No. EP/N027671/1 and EP/N034872/1. Work at Ural Federal University was supported by the Russian Science Foundation under Grant No. 18-12-00185. G. C. was supported by the U. S. National Science Foundation under Grant No. DMR-1712101. The IXS experiments were performed at beamline BL43LXU at the SPring-8 synchrotron with the approval of RIKEN under Proposal No. 20180059.

Appendix: Density Functional Theory Calculations

The DFT calculation in the LDA discussed above did not take into account the effects SOC, U or the magnetic structure, and therefore does not predict an electronic structure in agreement with the known spin-orbit assisted Mott insulating state of parent Sr_2IrO_4 (the metallic ground state that it predicts is in fact a better description of the doped compound). We repeated this calcu-

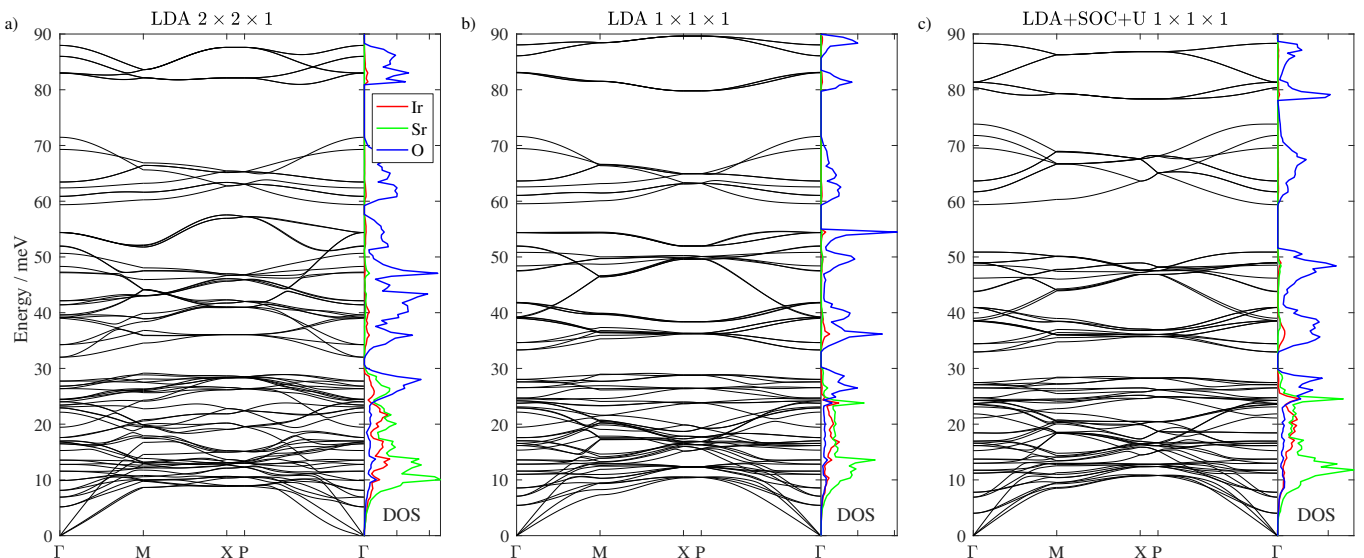


FIG. 5. Phonon band structures (black lines) and projected phonon DOS for Ir (red), Sr (green) and O (blue), calculated a) in the LDA approximation on a $2 \times 2 \times 1$ supercell, b) in the LDA approximation on a $1 \times 1 \times 1$ supercell, and c) with LDA+SOC+U on a $1 \times 1 \times 1$ supercell. The addition of SOC+U results in small changes in the phonon dispersions, most prominently in the O modes above 30 meV, while the increasing the cell size leads to far more significant changes.

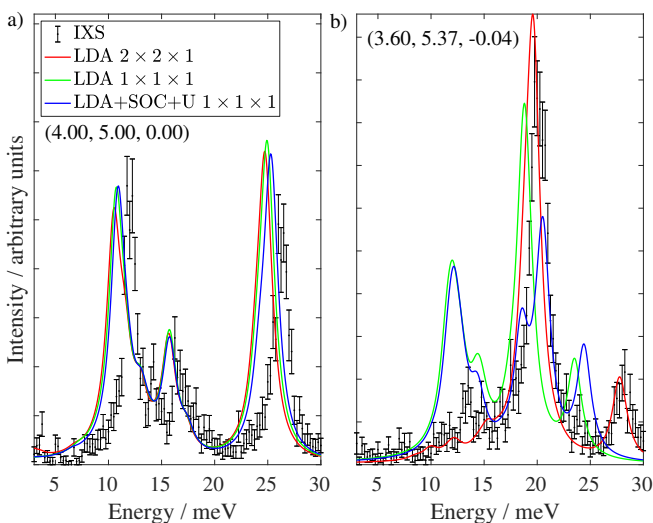


FIG. 6. Comparison of IXS spectra (black points) to $S(\mathbf{Q}, \omega)$ calculated with LDA on a $2 \times 2 \times 1$ supercell (red), LDA on a $1 \times 1 \times 1$ supercell (green), and LDA+SOC+U on a $1 \times 1 \times 1$ supercell (blue) at momentum transfers of a) $(4, 5, 0)$ and b) $(3.60, 5.37, -0.04)$. At the zone center the calculations differ by only a small shift in the mode energies, while further out in the Brillouin zone the $1 \times 1 \times 1$ supercell calculations predict intense modes that are not present in the experimental data.

lation including SOC+U, using $U = 3.05$ eV and $J = 0.48$ eV to reproduce the measured charge gap⁴⁴, and the non-collinear antiferromagnetic structure given by Ye *et*

*al.*³³. Due to the additional memory requirements of this, however, the supercell had to be reduced to $1 \times 1 \times 1$.

Figure 5 shows the phonon band structures and projected DOS for these two calculations, as well as for an LDA calculation on a $1 \times 1 \times 1$ supercell for comparison. Comparing the calculations on the minimal unit cell in Fig. 5b and c, it can be seen that the addition of SOC+U mostly affects the O modes above 30 meV, whose IXS intensities were too low to be measured in this work. Comparing these to the LDA calculation on the larger supercell in Fig. 5a, by contrast, shows more significant changes across all of the modes.

We also calculated the dynamic structure factor for these three different cases in order to compare with our IXS measurements. Figure 6 shows this comparison at two representative momentum transfers. At the zone centre the supercell size should be of minimal importance, and Fig. 6a shows that the calculations differ by only a small shift in the mode energies (~ 0.5 meV) and intensities. Further out into the Brillouin zone, however, the supercell size becomes critical, with the calculations on the minimal supercell showing prominent modes that are not present in the IXS spectra (Fig. 6b).

These comparisons highlight the inadequacy of the minimal supercell in simulating the lattice dynamics of Sr_2IrO_4 . In $5d$ oxides with large unit cells such as these, therefore, where LDA+SOC+U calculations involving non-collinear magnetic structures are prohibitively computationally demanding for larger supercells, a DFT perturbation approach may be more suitable.

* cameron.dashwood.17@ucl.ac.uk

¹ G. Jackeli and G. Khaliullin, *Phys. Rev. Lett.* **102**, 2

- (2009).
- ² W. Witzczak-Krempa, G. Chen, Y. B. Kim, and L. Balents, *Annu. Rev. Condens. Matter Phys.* **5**, 57 (2014).
 - ³ G. Cao and P. Schlottmann, *Reports Prog. Phys.* **81** (2018).
 - ⁴ J. Bertinshaw, Y. Kim, G. Khaliullin, and B. Kim, *Annu. Rev. Condens. Matter Phys.* **10**, 315 (2018).
 - ⁵ B. J. Kim, H. Jin, S. J. Moon, J.-Y. Kim, B.-G. Park, C. S. Leem, J. Yu, T. W. Noh, C. Kim, S.-J. Oh, J.-H. Park, V. Durairaj, G. Cao, and E. Rotenberg, *Phys. Rev. Lett.* **101**, 76402 (2008).
 - ⁶ B. J. Kim, H. Ohsumi, T. Komesu, S. Sakai, T. Morita, H. Takagi, and T. Arima, *Science (80-.)*. **323**, 1329 (2009).
 - ⁷ M. K. Crawford, M. A. Subramanian, R. L. Harlow, J. A. Fernandez-Baca, Z. R. Wang, and D. C. Johnston, *Phys. Rev. B* **49**, 9198 (1994).
 - ⁸ F. Wang and T. Senthil, *Phys. Rev. Lett.* **106**, 136402 (2011).
 - ⁹ J. Kim, D. Casa, M. H. Upton, T. Gog, Y.-j. Kim, J. F. Mitchell, M. V. Veenendaal, M. Daghofer, J. V. D. Brink, G. Khaliullin, and B. J. Kim, *Phys. Rev. Lett.* **108**, 177003 (2012).
 - ¹⁰ S. Boseggia, R. Springell, H. C. Walker, H. M. Rønnow, C. Rüegg, H. Okabe, M. Isobe, R. S. Perry, S. P. Collins, and D. F. McMorrow, *Phys. Rev. Lett.* **110**, 117207 (2013).
 - ¹¹ D. Pincini, J. G. Vale, C. Donnerer, A. De La Torre, E. C. Hunter, R. Perry, M. Moretti Sala, F. Baumberger, and D. F. McMorrow, *Phys. Rev. B* **96** (2017).
 - ¹² Y. K. Kim, O. Krupin, J. D. Denlinger, A. Bostwick, E. Rotenberg, Q. Zhao, J. F. Mitchell, J. W. Allen, and B. J. Kim, *Science (80-.)*. **345**, 187 (2014).
 - ¹³ Y. K. Kim, N. H. Sung, J. D. Denlinger, and B. J. Kim, *Nat. Phys.* **12**, 37 (2015).
 - ¹⁴ H. Liu and G. Khaliullin, *Phys. Rev. Lett.* **122**, 57203 (2019).
 - ¹⁵ J. Porras, J. Bertinshaw, H. Liu, G. Khaliullin, N. H. Sung, J.-W. Kim, S. Francoual, P. Steffens, G. Deng, M. M. Sala, A. Efimenko, A. Said, D. Casa, X. Huang, T. Gog, J. Kim, B. Keimer, and B. J. Kim, *Phys. Rev. B* **99**, 085125 (2019).
 - ¹⁶ H. Gretarsson, N. H. Sung, M. Höppner, B. J. Kim, B. Keimer, and M. Le Tacon, *Phys. Rev. Lett.* **116**, 136401 (2016).
 - ¹⁷ J. M. Tranquada, B. J. Sternlieb, J. D. Axe, Y. Nakamura, and S. Uchida, *Nature* **375**, 561 (1995).
 - ¹⁸ R. Comin and A. Damascelli, *Annu. Rev. Condens. Matter Phys.* **7**, 369 (2016).
 - ¹⁹ J. Zaanen and O. Gunnarsson, *Phys. Rev. B* **40**, 7391 (1989).
 - ²⁰ D. Poilblanc and T. M. Rice, *Phys. Rev. B* **39**, 9749 (1989).
 - ²¹ X. Chen, J. L. Schmeh, Z. Islam, Z. Porter, E. Zoghlin, K. Finkelstein, J. P. Ruff, and S. D. Wilson, *Nat. Commun.* **9** (2018).
 - ²² H. Chu, L. Zhao, A. De La Torre, T. Hogan, S. D. Wilson, and D. Hsieh, *Nat. Mater.* **16**, 200 (2017).
 - ²³ W. Jin, S. Li, J. Liu, Q. Han, Z. Porter, C. Peterson, J. Schmeh, I. Boulares, K. Sun, R. Merlin, S. D. Wilson, and L. Zhao, *Phys. Rev. B* **99**, 41109 (2019).
 - ²⁴ F. Weber, S. Rosenkranz, J.-P. Castellan, R. Osborn, R. Hott, R. Heid, K.-P. Bohnen, T. Egami, A. H. Said, and D. Reznik, *Phys. Rev. Lett.* **107**, 107403 (2011).
 - ²⁵ D. Reznik, L. Pintschovius, M. Ito, S. Iikubo, M. Sato, H. Goka, M. Fujita, K. Yamada, G. D. Gu, and J. M. Tranquada, *Nature* **440**, 1170 (2006).
 - ²⁶ H. Miao, D. Ishikawa, R. Heid, M. Le Tacon, G. Fabbri, D. Meyers, G. D. Gu, A. Q. Baron, and M. P. Dean, *Phys. Rev. X* **8** (2018).
 - ²⁷ A. Q. R. Baron, in *Synchrotron Light Sources Free. Lasers Accel. Physics, Instrum. Sci.*, edited by E. J. Jaeschke, S. Khan, J. R. Schneider, and J. B. Hastings (Springer International Publishing, Cham, 2016) pp. 1643–1757. See also arXiv 1504.01098.
 - ²⁸ A. de la Torre, S. McKeown Walker, F. Y. Bruno, S. Riccò, Z. Wang, I. Gutierrez Lezama, G. Scheerer, G. Giriat, D. Jaccard, C. Berthod, T. K. Kim, M. Hoesch, E. C. Hunter, R. S. Perry, A. Tamai, and F. Baumberger, *Phys. Rev. Lett.* **115**, 176402 (2015).
 - ²⁹ P. E. Blöchl, *Phys. Rev. B* **50**, 17953 (1994).
 - ³⁰ G. Kresse and J. Furthmüller, *Phys. Rev. B* **54**, 11169 (1996).
 - ³¹ J. P. Perdew and Y. Wang, *Phys. Rev. B* **45**, 13244 (1992).
 - ³² A. Togo and I. Tanaka, *Scr. Mater.* **108**, 1 (2015).
 - ³³ F. Ye, S. Chi, B. C. Chakoumakos, J. A. Fernandez-Baca, T. Qi, and G. Cao, *Phys. Rev. B* **87**, 140406 (2013).
 - ³⁴ A. Q. R. Baron, *SPRING-8 Inf. Newsl.* **15**, 14 (2010).
 - ³⁵ S. B. Wilkins, M. P. M. Dean, J. Fink, M. Hücker, J. Geck, V. Soltwisch, E. Schierle, E. Weschke, G. Gu, S. Uchida, N. Ichikawa, J. M. Tranquada, and J. P. Hill, *Phys. Rev. B* **84**, 195101 (2011).
 - ³⁶ L. Pintschovius, N. Pyka, W. Reichardt, A. Rumiantsev, N. L. Mitrofanov, A. S. Ivanov, G. Collin, and P. Bourges, *Phys. C Supercond.* **185-189**, 156 (1991).
 - ³⁷ R. J. McQueeney, Y. Petrov, T. Egami, M. Yethiraj, G. Shirane, and Y. Endoh, *Phys. Rev. Lett.* **82**, 628 (1999).
 - ³⁸ H. Uchiyama, A. Q. R. Baron, S. Tsutsui, Y. Tanaka, W.-Z. Hu, A. Yamamoto, S. Tajima, and Y. Endoh, *Phys. Rev. Lett.* **92**, 197005 (2004).
 - ³⁹ D. Reznik, T. Fukuda, D. Lamago, A. Q. R. Baron, S. Tsutsui, M. Fujita, and K. Yamada, *J. Phys. Chem. Solids* **69**, 3103 (2008).
 - ⁴⁰ J. Graf, M. D’Astuto, C. Jozwiak, D. R. Garcia, N. L. Saini, M. Krisch, K. Ikeuchi, A. Q. R. Baron, H. Eisaki, and A. Lanzara, *Phys. Rev. Lett.* **100**, 227002 (2008).
 - ⁴¹ M. D’Astuto, G. Dhalle, J. Graf, M. Hoesch, P. Giura, M. Krisch, P. Berthet, A. Lanzara, and A. Shukla, *Phys. Rev. B* **78**, 140511 (2008).
 - ⁴² M. Le Tacon, A. Bosak, S. M. Souliou, G. Dellea, T. Loew, R. Heid, K.-P. Bohnen, G. Ghiringhelli, M. Krisch, and B. Keimer, *Nat. Phys.* **10**, 52 (2013).
 - ⁴³ V. Sadovnichy, A. Tikhonravov, V. Voevodin, and V. Opanasenko, in *Contemp. High Perform. Comput. From Petascale Towar. Exascale*, edited by J. S. Vetter (CRC Press, Boca Raton, 2013) pp. 283–307.
 - ⁴⁴ I. V. Solovye, V. V. Mazurenko, and A. A. Katanin, *Phys. Rev. B* **92**, 235109 (2015).

Supplemental Material: Momentum-resolved lattice dynamics of parent and electron-doped Sr_2IrO_4

C. D. Dashwood,^{1,*} H. Miao,² J. G. Vale,¹ D. Ishikawa,³ D. A. Prishchenko,⁴
V. V. Mazurenko,⁴ V. G. Mazurenko,⁴ R. S. Perry,¹ G. Cao,⁵ A. de la Torre,^{6,7}
F. Baumberger,⁷ A. Q. R. Baron,³ D. F. McMorrow,¹ and M. P. M. Dean²

¹*London Centre for Nanotechnology and Department of Physics and Astronomy,
University College London, Gower Street, London WC1E 6BT, UK*

²*Department of Condensed Matter Physics and Materials Science,
Brookhaven National Laboratory, Upton, New York 11973, USA*

³*Materials Dynamics Laboratory, RIKEN SPring-8 Center,
RIKEN, Sayo Hyogo 697-5148, Japan*

⁴*Department of Theoretical Physics and Applied Mathematics,
Ural Federal University, 19 Mira Street, Ekaterinburg 620002, Russia*

⁵*Department of Physics, University of Colorado at Boulder, Boulder, Colorado 80309, USA*

⁶*Institute for Quantum Information and Matter and Department of Physics,
California Institute of Technology, Pasadena, California 91125, USA*

⁷*Department of Quantum Matter Physics, University of Geneva,
24 Quai Ernest-Ansermet, 1211 Geneva 4, Switzerland*

(Dated: December 15, 2024)

I. DYNAMIC STRUCTURE FACTOR CALCULATIONS

The intensity measured in non-resonant inelastic x-ray scattering (IXS) at total momentum transfer \mathbf{Q} and energy loss ω is directly proportional to the dynamic structure factor $S(\mathbf{Q}, \omega)$, with the constant of proportionality depending on the momenta and polarisation of the incoming/outgoing photons¹. Away from Bragg reflections, $S(\mathbf{Q}, \omega)$ is dominated by the one-phonon term, which in the Born approximation reads

$$S(\mathbf{Q}, \omega) = \sum_{\mathbf{q}, j} |F(\mathbf{Q}, \mathbf{q}, j)|^2 \langle n_{qj} + 1 \rangle \delta(\omega - \omega_{qj}) \delta(\mathbf{Q} - \mathbf{q}) \quad (\text{S1})$$

where \mathbf{q} sums over the reduced momenta in the first Brillouin zone, and j sums over the $3n$ modes at \mathbf{q} (n being the number of atoms in the primitive unit cell) with frequencies ω_{qj} and Bose factors $\langle n_{qj} + 1 \rangle = (1 - e^{-\omega_{qj}/(k_b T)})^{-1}$. F is given by

$$F(\mathbf{Q}, \mathbf{q}, j) = \sum_d \sqrt{\frac{f_d(\mathbf{Q})}{2m_d \omega_{qj}}} e^{-W_d(\mathbf{Q})} e^{-i\mathbf{Q} \cdot \mathbf{r}_d} \mathbf{Q} \cdot \mathbf{e}_{qjd} \quad (\text{S2})$$

where d sums over the n atoms in the primitive unit cell with masses m_d located at \mathbf{r}_d , $e^{-W_d(\mathbf{Q})}$ is the Debye-Waller factor, \mathbf{e}_{qjd} the complex phonon polarisation, and $f_d(\mathbf{Q})$ the x-ray form factor².

Equation S1 was evaluated using the PHONOPY package³. In order to be directly compared with our IXS data, however, a finite linewidth γ_{qj} (due mostly to instrument resolution) must be introduced by replacing the frequency delta function with a damped harmonic oscillator lineshape

$$\delta(\omega - \omega_{qj}) \rightarrow \chi_j''(\mathbf{q}, \omega) = \frac{4\omega\omega_{qj}\gamma_{qj}}{\pi \left[(\omega^2 - \omega_{qj}^2 - \gamma_{qj}^2)^2 + 4\omega^2\gamma_{qj}^2 \right]}. \quad (\text{S3})$$

We use $\gamma_{qj} = \gamma = 0.8 \text{ meV}$ for all modes at all momenta.

II. COMPARISON WITH RAMAN MEASUREMENTS

Here we compare our LDA calculation on the $2 \times 2 \times 1$ supercell with previously published Raman and infra-red (IR) spectroscopy studies. The primitive unit cell of Sr_2IrO_4 contains 28 atoms, giving 84 phonon modes. A symmetry analysis of the $I4_1/acd$ space group with Ir atoms at Wyckoff site $8a$, Sr at $16d$ and O at $16d$ (apical) and $16f$ (basal) shows that the Raman active modes have irreducible representations $3A_{1g} + 5B_{1g} + 4B_{2g} + 13E_g$ and the IR modes have irreducible representations $5A_{2u} + 13E_u$, leaving $4A_{1u} + 4A_{2g} + 4B_{1u} + 3B_{2u}$. Table S1 shows that our calculated mode energies compare well to the Raman and IR studies.

LDA $2 \times 2 \times 2$			Ref. 4	Ref. 5 (Raman)		Ref. 6 (IR)	
Band	Assignment	Calculated	Calculated	Calculated	Observed	Calculated	Observed
1, 2	E_u	Acoustic	Acoustic	-	-	-	-
3	A_{2u}	Acoustic	Acoustic	-	-	-	-
4, 5	E_u	42	Imaginary	-	-	30	-
6, 7	E_g	56	Imaginary	-	-	-	-
8, 9	E_g	66	53	-	-	-	-
10, 11	E_u	80	84	-	-	81	103
12, 13	E_g	93	91	-	-	-	-
14, 15	E_u	103	101	-	-	92	115
16, 17	E_g	109	108	-	-	-	-
18	B_{1g}	123	114	110	-	-	-
19, 20	E_g	133	132	-	-	-	-
21, 22	E_u	135	120	-	-	122	138
23	B_{2g}	137	134	135	-	-	-
24	A_{1u}	137	-	-	-	-	-
25	A_{2g}	142	-	-	-	-	-
26	B_{1u}	142	-	-	-	-	-
27	B_{2u}	157	-	-	-	-	-
28	B_{1g}	179	167	168	-	-	-
29	A_{1u}	185	-	-	-	-	-
30	B_{2g}	185	173	-	-	-	-

31	A_{2u}	186	172	-	-	172	192
32, 33	E_u	189	174	-	-	178	-
34, 35	E_g	194	186	171	191	-	-
36, 37	E_u	197	194	-	-	186	-
38	A_{1g}	198	181	188	188	-	-
39, 40	E_g	213	203	-	-	-	-
41, 42	E_u	216	204	-	-	212	214
43, 44	E_g	224	205	-	-	-	-
45, 46	E_u	258	257	-	-	251	270
47, 48	E_g	276	266	-	-	-	-
49	B_{2u}	315	-	-	-	-	-
50, 51	E_g	315	291	-	-	-	-
52	A_{1g}	316	260	326	278	-	-
53, 54	E_u	319	293	-	-	298	283
55, 56	E_g	334	314	-	-	-	-
57, 58	E_u	340	314	-	-	323	324
59	A_{2g}	380	-	-	-	-	-
60	B_{1u}	381	-	-	-	-	-
61	A_{2u}	390	340	-	-	374	373
62	B_{1g}	409	359	391	-	-	-
63	A_{1u}	419	-	-	-	-	-
64	B_{2g}	419	371	410	395	-	-
65, 66	E_u	439	381	-	-	406	367
67, 68	E_g	439	380	-	-	-	-
69	A_{2u}	479	502	-	-	443	515
70	B_{2g}	491	513	457	495	-	-
71	A_{1u}	491	-	-	-	-	-
72	B_{2u}	503	-	-	-	-	-
73	B_{1u}	512	-	-	-	-	-
74	A_{2g}	512	-	-	-	-	-

75	A_{1g}	559	588	532	562	-	-
76	B_{1g}	576	596	546	-	-	-
77, 78	E_u	669	751	-	-	645	664
79, 80	E_g	670	751	-	-	-	-
81	B_{1g}	694	808	660	693	-	-
82	A_{2u}	694	808	-	-	660	-
83	B_{1u}	709	-	-	-	-	-
84	A_{2g}	709	-	-	-	-	-

TABLE S1: Comparison of the modes calculated with LDA on a $2 \times 2 \times 1$ supercell to those from previously published Raman and IR studies on Sr_2IrO_4 . All frequencies are in cm^{-1} . The imaginary frequencies in Ref. 4 arise from their use of the unrelaxed experimental crystal structure.

III. SUPPLEMENTAL DATA FOR THE PARENT AND DOPED COMPOUNDS

Here we present IXS spectra and LDA calculations on the $2 \times 2 \times 1$ supercell for the \mathbf{Q} points indicated in Fig. ?? but not shown in the main text. The conclusions drawn in the main text (namely the good agreement between the experimental spectra and non-magnetic DFT calculations, and the lack of any visible anomalous frequency or linewidth changes through T_N) apply equally well to these data.

* cameron.dashwood.17@ucl.ac.uk

¹ A. Q. R. Baron, *J. Spectrosc. Soc. Japan* **58**, 205 (2009).

² D. Waasmaier and A. Kirfel, *Acta Crystallogr. Sect. A* **51**, 416 (1995).

³ A. Togo and I. Tanaka, *Scr. Mater.* **108**, 1 (2015).

⁴ K. Samanta, F. M. Ardito, N. M. Souza-Neto, and E. Granado, *Phys. Rev. B* **98**, 094101 (2018).

⁵ H. Gretarsson, J. Saucedo, N. H. Sung, M. Höppner, M. Minola, B. J. Kim, B. Keimer, and M. Le Tacon, *Phys. Rev. B* **96**, 1 (2017).

⁶ D. Pröpper, A. N. Yaresko, M. Höppner, Y. Matiks, Y.-L. Mathis, T. Takayama, A. Matsumoto, H. Takagi, B. Keimer, and A. V. Boris, *Phys. Rev. B* **94**, 035158 (2016).

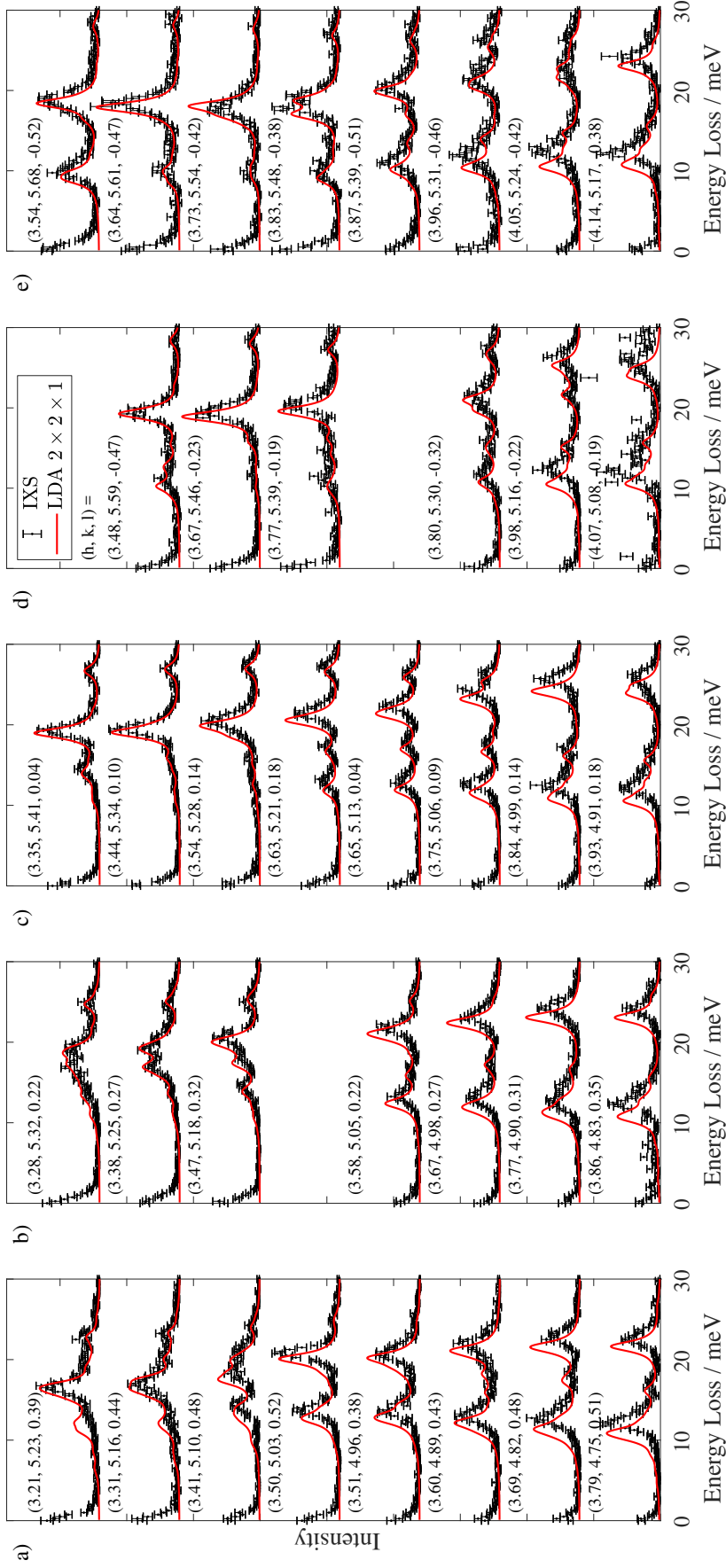


FIG. S1. IXS spectra in the parent compound at 100 K for each vertical column of analysers not shown in the main text (black points) compared to the dynamic structure factor calculated with LDA on a $2 \times 2 \times 1$ supercell (solid red lines). The spectra in each plot are offset vertically for clarity. The missing spectra are due to detector malfunctions.

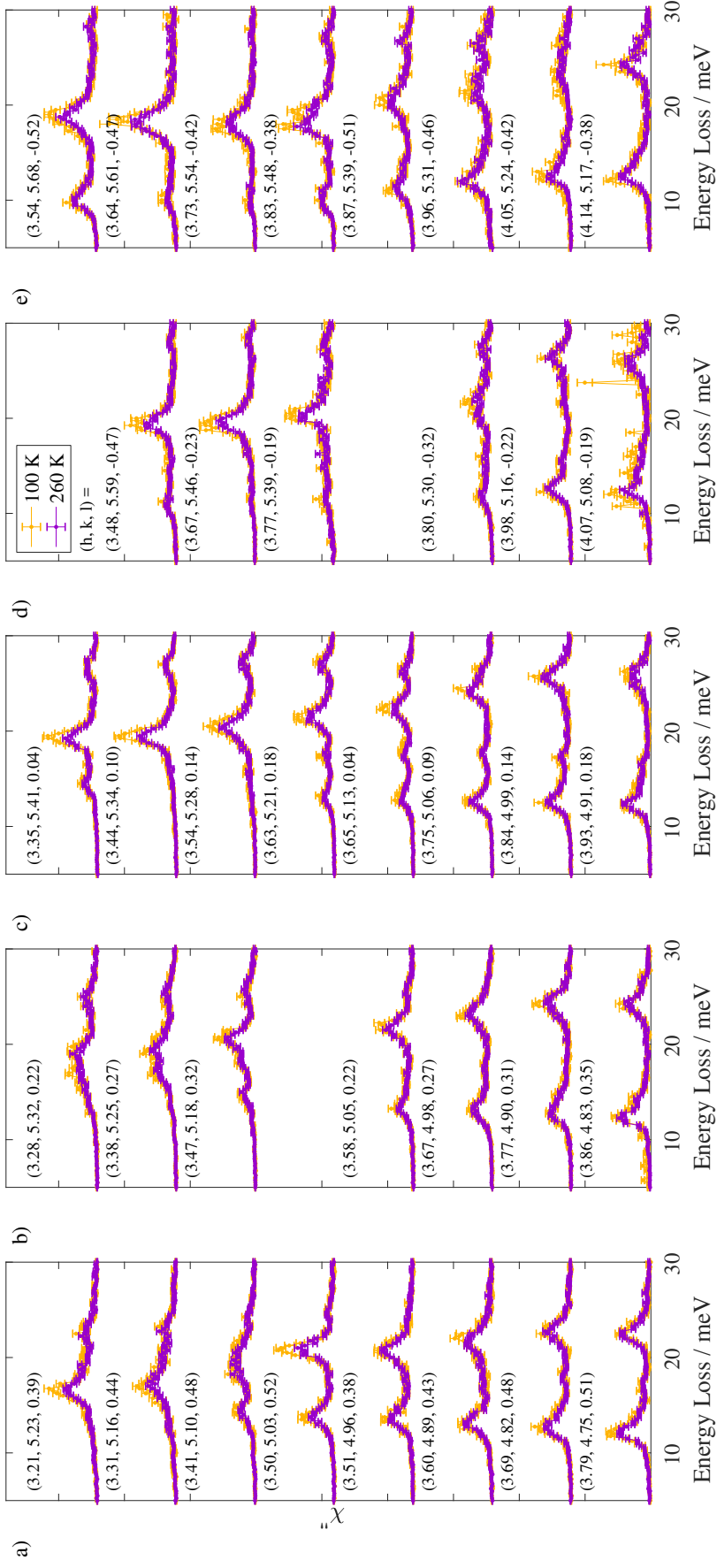


FIG. S2. Bose-factor corrected IXS spectra in the parent compound at 100 K (orange) and 260 K (purple) for each vertical column of analysers not shown in the main text. The spectra in each plot are offset vertically for clarity. The missing spectra are due to detector malfunctions.

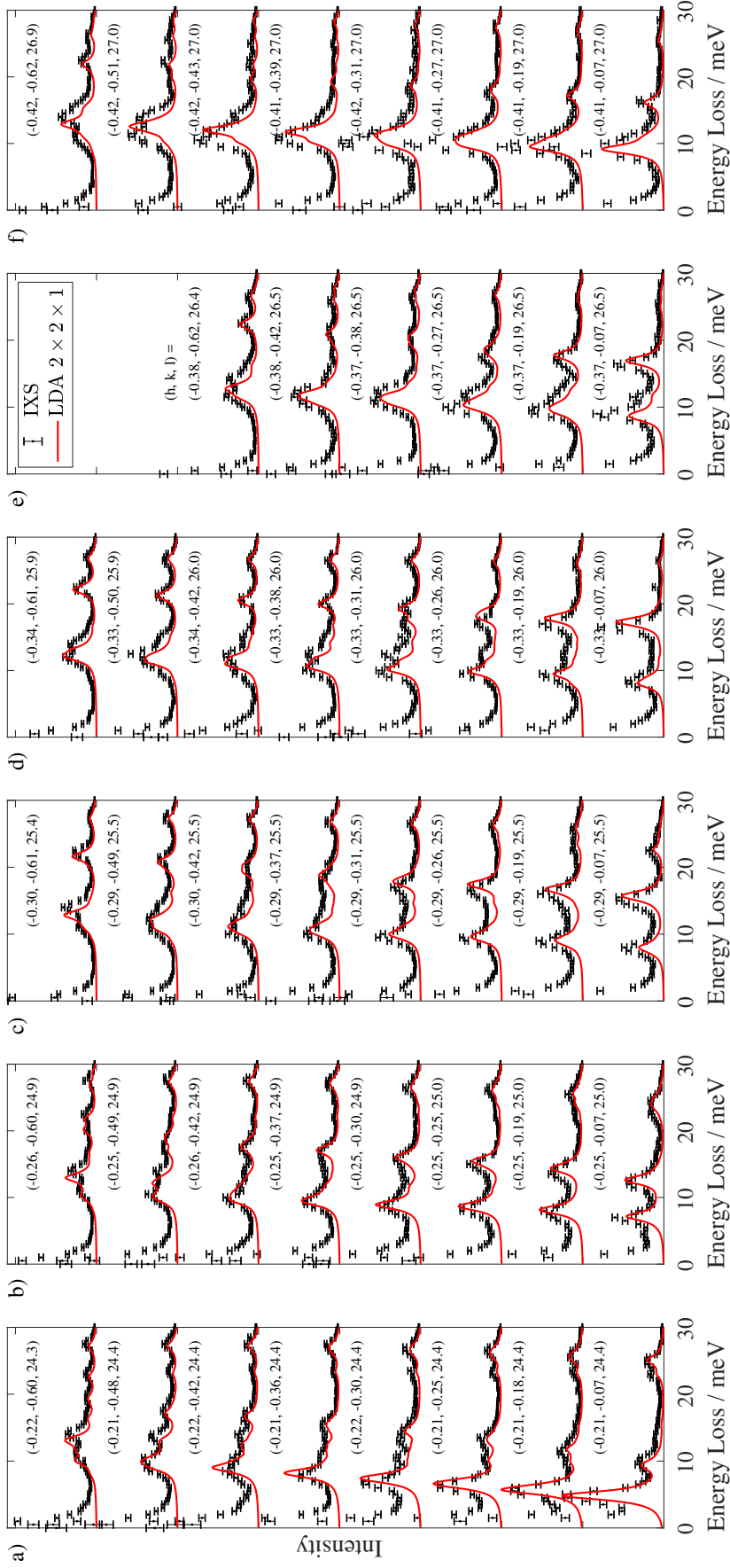


FIG. S3. IXS spectra in the doped compound at 9 K for each vertical column of analysers not shown in the main text (black points) compared to the dynamic structure factor calculated with LDA on a $2 \times 2 \times 1$ supercell (solid red lines). The spectra in each plot are offset vertically for clarity. The missing spectra are due to detector malfunctions.

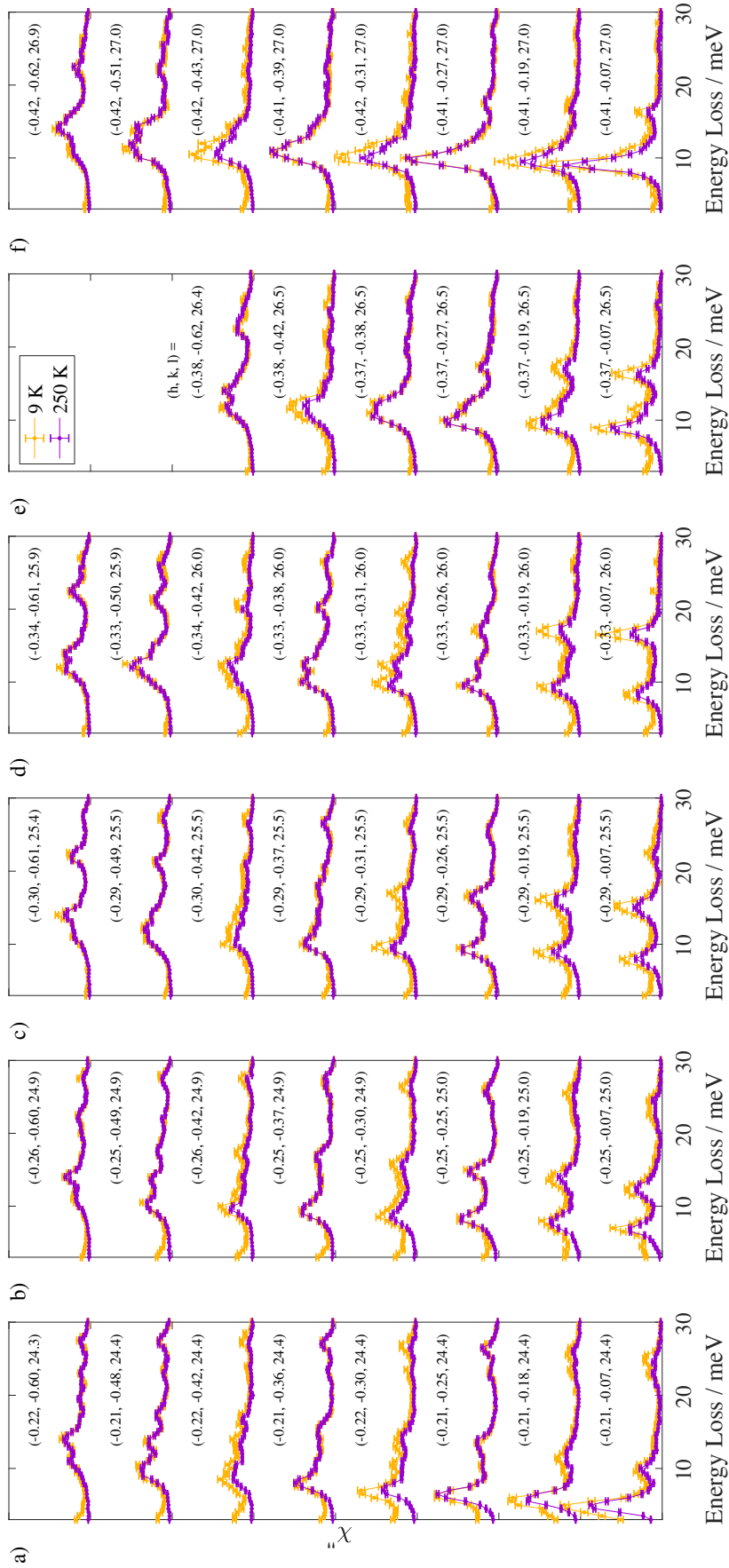


FIG. S4. Bose-factor corrected IXS spectra in the doped compound at 9 K (orange) and 250 K (purple) for each vertical column of analysers not shown in the main text. The spectra in each plot are offset vertically for clarity. The missing spectra are due to detector malfunctions.

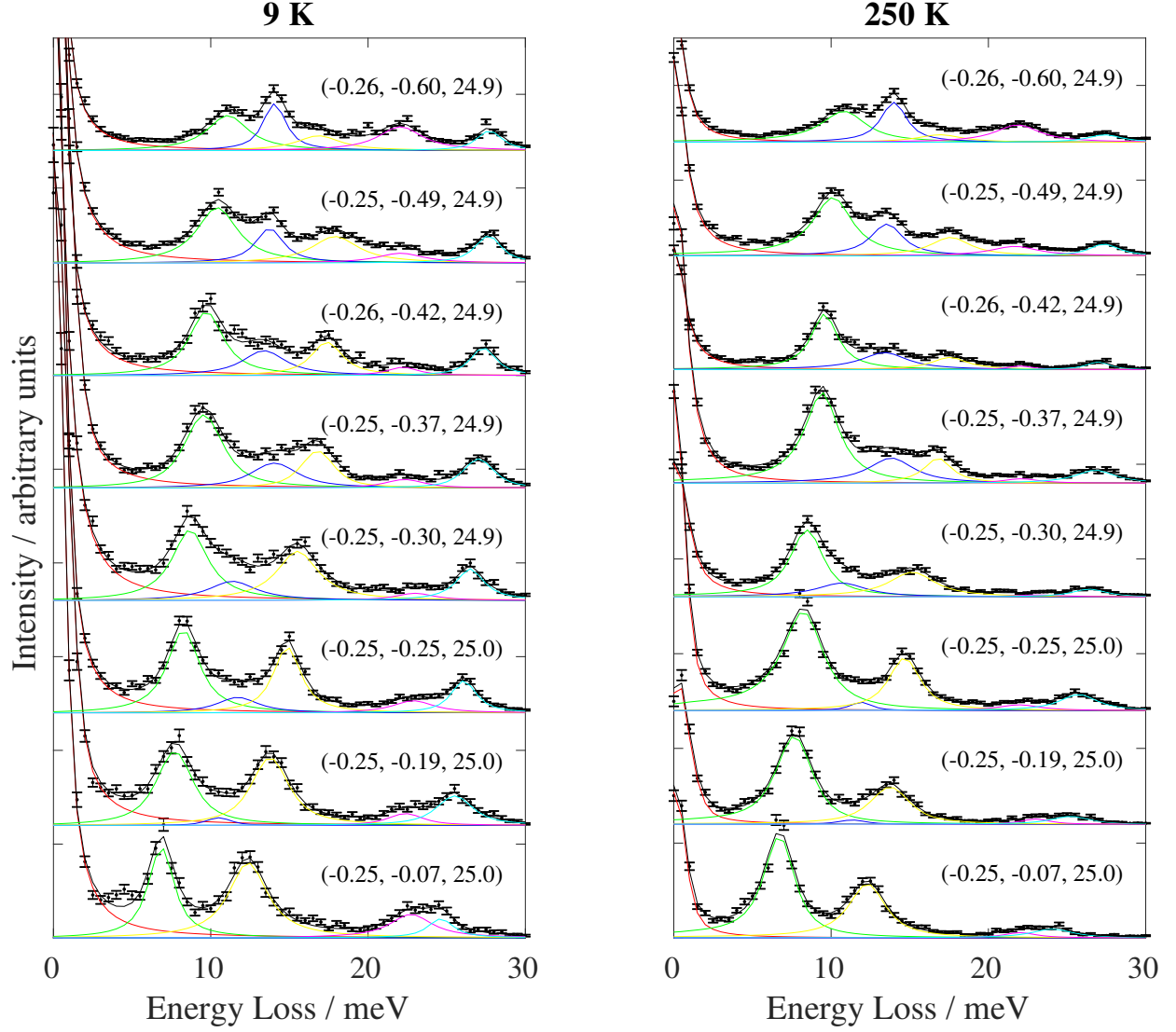


FIG. S5. Detail of the fits (black line) of the doped spectra (black points). As described in the main text, the elastic peak is fitted with a pseudo-Voigt resolution function (red), while each of the phonon modes is fitted with a damped harmonic oscillator lineshape weighted by the Bose factor and convoluted with the resolution function (green, blue, yellow, magenta and cyan respectively for each mode).